

Structural and electrical analysis of epitaxial 2D/3D vertical heterojunctions of monolayer MoS₂ on GaN

Terrance P. O'Regan,^{1,(a),b)} Dmitry Ruzmetov,^{1,b)} Mahesh R. Neupane,¹ Robert A. Burke,¹ Andrew A. Herzing,² Kehao Zhang,³ A. Glen Birdwell,¹ DeCarlos E. Taylor,⁴ Edward F. C. Byrd,⁴ Scott D. Walck,⁴ Albert V. Davydov,² Joshua A. Robinson,³ and Tony G. Ivanov¹

¹*Sensors and Electron Devices Directorate, U.S. Army Research Laboratory, Adelphi, Maryland 20783, USA*

²*Material Measurement Laboratory, National Institute of Standards and Technology, Gaithersburg, Maryland 20899, USA*

³*Department of Materials Science and Engineering and Center for Two-Dimensional and Layered Materials, The Pennsylvania State University, University Park, Pennsylvania 16802, USA*

⁴*Weapons and Materials Research Directorate, U.S. Army Research Laboratory, Aberdeen Proving Ground, Maryland 21005, USA*

(Received 17 April 2017; accepted 13 July 2017; published online 4 August 2017)

Integration of two-dimensional (2D) and conventional (3D) semiconductors can lead to the formation of vertical heterojunctions with valuable electronic and optoelectronic properties. Regardless of the growth stacking mechanism implemented so far, the quality of the formed heterojunctions is susceptible to defects and contaminations mainly due to the complication involved in the transfer process. We utilize an approach that aims to eliminate the transfer process and achieve epitaxial vertical heterojunctions with low defect interfaces necessary for efficient vertical transport. Monolayers of MoS₂ of approximately 2 μm domains are grown epitaxially by powder vaporization on GaN substrates forming a vertical 2D/3D heterojunction. Cross-sectional transmission electron microscopy (XTEM) is employed to analyze the in-plane lattice constants and van der Waals (vdW) gap between the 2D and 3D semiconductor crystals. The extracted in-plane lattice mismatch between monolayer MoS₂ and GaN is only 1.2% which corresponds well to the expected mismatch between bulk MoS₂ and GaN. The vdW gap between MoS₂ and GaN, extracted from the XTEM measurements, is consistent with the vdW gap of 3.1 Å predicted by our first principles calculations. The effect of monolayer (1L) MoS₂ on the electrical characteristics of 2D/3D semiconductor heterojunctions was studied using conductive atomic force microscopy (CAFM). The electrical current across the CAFM-tip/1L-MoS₂/GaN vertical junctions is dominated by the tip/GaN interface of both *n*- and *p*-doped GaN. This electronic transparency of 1L-MoS₂ tells us that a 2D crystal component has to be above a certain thickness before it can serve as an independent semiconductor element in 2D/3D heterojunctions. [<http://dx.doi.org/10.1063/1.4997188>]

In recent years, the exponential growth of research on 2D materials such as graphene, MoS₂, and h-BN has elucidated important physics and devices.¹ However, the ability to obtain large-area, high-quality materials presents an inherent obstacle to the realization of technologies based on 2D materials. In some cases, 2D materials have been grown partially aligned on sapphire but require subsequent transfer to the substrate of interest, resulting in potential contamination issues.² Avoiding the transfer step, we have previously grown MoS₂ on *n*-doped GaN via powder vaporization and provided scanning electron microscopy (SEM) images showing the evidence of epitaxial alignment,³ and others have grown MoS₂ on *p*-doped InGaN.⁴ In these cases, the GaN substrate acts as a template for epitaxial growth and as an active element in the 2D/3D heterojunction, opening up the possibility of vertical electronic and optoelectronic devices.^{3,5-7} Here, we focus on the quantitative structural analysis of a 2D/3D heterojunction using cross-sectional transmission electron microscopy (XTEM), density functional theory (DFT) calculations, and electrical characterization of MoS₂ grown on *n*- and *p*-doped GaN.

To understand the nature of the epitaxial MoS₂/GaN interface, we performed XTEM to extract in-plane lattice constants and characterize the van der Waals (vdW) gap. XTEM revealed a close lattice match of 1.2% between MoS₂ and GaN with the lattice constants near their bulk material values, indicating that minimal strain is expected in the 2D/3D heterostructure. The latter is important for building more complex heterostructures based on these materials in the future. The observed MoS₂-GaN vdW gap of ~3.1 Å is consistent with our DFT prediction. In addition, monolayer MoS₂ on both the *n*-type and *p*-type GaN was synthesized to form 2D/3D heterojunctions, and the electrical conductivity across these junctions was analyzed using conductive atomic force microscopy (CAFM). Our results suggest that a single monolayer of MoS₂ does not act as an independent *n*-type semiconductor in a metal-tip/MoS₂/*p*-GaN heterojunction and only partially screens the metal CAFM tip from the *p*-GaN substrate. One important takeaway message when designing 2D/3D heterostructures is to ensure a sufficient thickness of each 2D semiconductor component (e.g., by taking a multilayer crystal), so that it can play its role in the *p*-*n* junction stack. Alternatively, the partial electronic transparency of a monolayer MoS₂ can be used to engineer the properties of the rest of the heterojunction device.

^{a)}Author to whom correspondence should be addressed: terrance.p.oregan.civ@mail.mil.

^{b)}T. P. O'Regan and D. Ruzmetov contributed equally to this work.

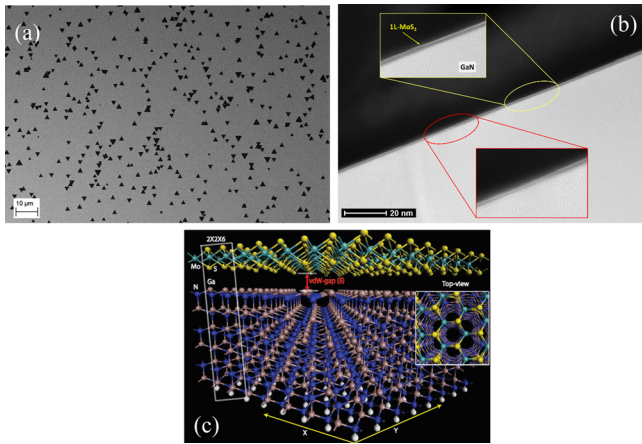


FIG. 1. MoS₂ domains on *n*-doped GaN. (a) SEM image showing MoS₂ triangles aligned with the GaN lattice. (b) Panoramic HAADF STEM image showing monolayer and bilayer MoS₂ on GaN and the overlapping character of the MoS₂ domain boundary. The upper inset shows single layer MoS₂ while the lower inset shows a grain boundary in the single layer MoS₂. (c) Optimized MoS₂/GaN supercell from DFT calculations. The calculated vdW gap is $\delta \sim 3.1$ Å. Atoms color code: yellow = S, green = Mo, blue = N, brown = Ga, and white = H.

Monolayer MoS₂ was grown on GaN substrates via a powder vaporization technique described previously.³ The GaN substrates, purchased from NTT-AT (Certain commercial instruments and materials are identified in this paper to foster understanding. Such identification does not imply recommendation or endorsement by the National Institute of Standards and Technology, nor does it imply that the equipment or materials identified are necessarily the best available for the purpose.), were *n*-doped and *p*-doped epitaxial GaN films grown by metalorganic chemical vapor deposition (MOCVD) on sapphire substrates. The thickness of *p*-doped GaN film was 1 μm with an Mg dopant concentration of 10¹⁹ cm⁻³ to achieve a free hole carrier density of 10¹⁷ cm⁻³. The *p*-GaN film was a single GaN layer which served

simultaneously as a part of the 2D/3D heterojunction and the bottom contact. The *n*-doped GaN film was a bilayer of *n*⁺-GaN (700 nm, free carrier $n = 10^{19}$ cm⁻³) and *n*-GaN (300 nm, $n = 10^{16}$ cm⁻³) on sapphire. The bottom *n*⁺-GaN layer was designed to serve as a bottom contact to the moderately doped top *n*-GaN layer. XTEM samples of two sapphire wafers with MoS₂/GaN layers were prepared by a traditional dimpling and ion milling technique.⁸ The specimen stack was built with two wafers, Sample A and Sample B, glued face to face and backed with blank silicon pieces to give a suitable thickness using EpoTek 353 ND epoxy from Epoxy Technology, Inc. Sample A was oriented with the (11 $\bar{2}$ 0) GaN plane parallel to the TEM cross-sectional plane (Figs. 1 and 2). Sample B was oriented with the (1 $\bar{1}$ 00) GaN plane along the cross-section (Fig. 2). After dicing and mechanical thinning, the samples were dimpled to approximately 10 μm using a Gatan dimple grinder. The samples were then ion milled to electron transparency using a Gatan PIPS-II ion mill with 5 keV Ar ions at 4° until perforation, followed by a final ion polishing at 500 eV for 10 min. Scanning transmission electron microscopy (STEM) was carried out using a spherical-aberration corrected FEI Titan 80–300 operating with a primary beam energy of 300 keV. High-angle annular dark-field (HAADF) images were collected using a detector inner collection angle of 70 mrad. Additionally, energy dispersive X-ray spectroscopy (XEDS) was carried out using a probe current of 0.3 nA and a side-entry silicon drift detector. The conductive atomic force microscopy (CAFM) measurements were performed on the Asylum Cypher high resolution atomic force microscope utilizing Pt-Ir, Pt, and doped diamond tips.

To elucidate our experimental observations on the 2D/3D heterojunction, we calculated interface properties using DFT with the projector augmented wave (PAW) method⁹ as implemented in the Vienna *Ab-initio* Simulation Package (VASP¹⁰) code. The structure optimization, total energy, and

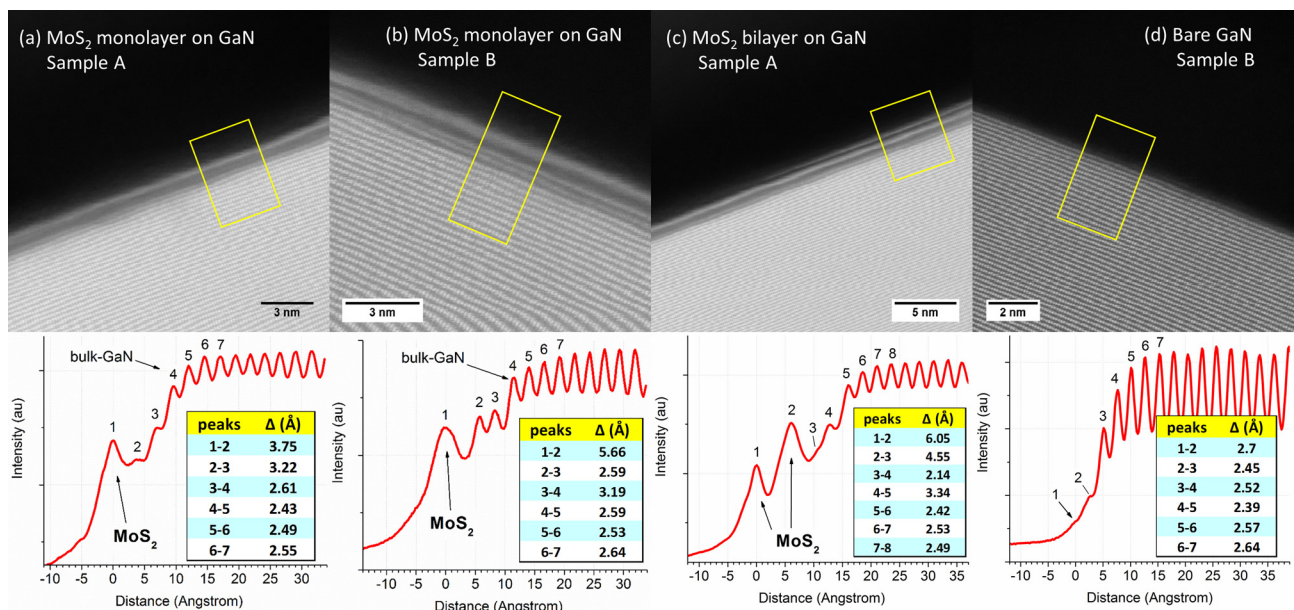


FIG. 2. XTEM images and peak intensity versus distance from the surface for (a) MoS₂ monolayer on GaN (Sample A), (b) MoS₂ monolayer on GaN (Sample B), (c) MoS₂ bilayer on GaN (Sample A), and (d) bare GaN (Sample B). Note: The intensities of the line profiles at each point from the yellow boxes in each of the XTEM images are obtained by summing the intensities along the width of the box, perpendicular to the line profile direction.

electronic structure calculations were performed using the generalized gradient approximation (GGA) parameterized by Perdew-Burke and Ernzerhof (PBE).¹¹ The kinetic energy cut-offs of 500 and 300 eV for electronic wave functions, for bulk GaN and MoS₂ respectively, were chosen and tested to reach convergence for the lattice properties. A Γ -centered Monkhorst-Pack Brillouin zone (BZ) integration scheme was adopted to integrate over the BZ.¹² The lattice parameters were optimized individually for bulk MoS₂ and wurtzite GaN. The semi-empirical DFT-D2 dispersion correction of Grimme was implemented to include the vdW interactions in the Kohn-Sham energies.¹³ The forces were calculated using the Hellmann-Feynman procedure and geometries were optimized using a conjugated gradient (CG) scheme. The atomic coordinates were optimized in all directions with a convergence criterion of 0.001 eV \AA^{-1} for the atomic forces. The optimized bulk MoS₂ lattice constants are $a = b = 3.19 \text{ \AA}$ and $c = 12.33 \text{ \AA}$, and bulk GaN lattice constants are $a = b = 3.22 \text{ \AA}$ and $c = 5.25 \text{ \AA}$. These values are in agreement with the experimental data for MoS₂: $a = b = 3.169 \text{ \AA}$ and $c = 12.324 \text{ \AA}$ (Ref. 14) and for GaN: $a = 3.189 \text{ \AA}$ and $c = 5.185 \text{ \AA}$.¹⁵

Using the optimized lattice parameters from our bulk calculations, a single layer MoS₂ (1L-MoS₂) and a GaN (0001) surface (s-GaN) were constructed, prior to forming 1L-MoS₂/s-GaN supercells [see Fig. 1(c)]. For both the systems, a vacuum spacing of 20 \AA was added along the z-axis to minimize spurious interactions with the central cell and its periodic images. In order to maintain a balance between accuracy and computational cost, a critical surface thickness that preserves bulk-like features was identified by varying the surface thickness in the out-of-plane direction (along z), while maintaining the periodicity of the in-plane directions (along x and y) and comparing the electronic properties, such as energy gap and edge states, to those of the bulk. The six Ga-N bilayers ($\sim 15 \text{ \AA}$) were found to be a suitable representation for the bulk-like GaN surface. In order to simulate the laterally contracted Ga bilayer structure under Ga-rich conditions, and also allow surface relaxation, a Ga surface consisting of a $(2 \times 2 \times 6)$ supercell with the in-plane and out-of-plane lattice constants of 6.4397 and 14.984 \AA , respectively, was modeled, where two Ga atoms were present in the outer laterally contracted over-layer for every one atom in the underlying layer resulting in a Ga-terminated surface. The dangling bonds at the N-terminated bottom layer were passivated by pseudo-H atoms with a charge of 0.75e in order to prevent an unphysical charge transfer between the top and the bottom slab surfaces. The upper three bilayers of s-GaN (0001) were allowed to relax, while the bottom three bilayers, and saturating H atoms, were fixed to mimic the bulk substrate. A vacuum spacing of 20 \AA was added along the z-axis for all the structures to minimize spurious interaction due to periodicity. For the electronic structure calculations, a $6 \times 6 \times 1$ k-mesh was used for both the monolayer MoS₂ and s-GaN (0001) structures. The k-mesh was reduced to a converged $3 \times 3 \times 1$ grid for the s-GaN and 1L-MoS₂/s-GaN supercell. Similarly, the energy cut-off for the plane wave basis was increased to 500 eV for the supercell calculations. The structure optimization parameters were similar to the bulk calculations mentioned previously. The 1L-MoS₂/s-GaN supercells were optimized with vdW

interactions included and resulted in a van der Waals gap (δ) of 3.1 \AA between the 1L-MoS₂ and s-GaN. Using the calculated self-consistent charges, we then calculate the band structure and density of states of the bulk GaN, 1L-MoS₂ and 1L-MoS₂/GaN systems. In order to rectify the limitation of the PBE method in underestimating the energy gap, we employ a hybrid functional (HSE06) as implemented in the VASP code.

The synthesized MoS₂ is observed in the form of triangular domains on *n*- or *p*-GaN (Fig. 1). The epitaxial alignment of MoS₂ with the GaN substrate results in a high uniformity in the orientation and shape of the 2D domains [Fig. 1(a)] unlike the typical in-plane randomly oriented MoS₂ domains grown on amorphous oxides.¹⁶ Overall, our MoS₂ was observed to be of single monolayer thickness by Raman measurements³ and XTEM [Fig. 1(b)]. The average lateral size of the monolayer domain ranges between 1 μm and 3 μm depending on the growth run. There is occasional bilayer growth and higher order stacks in the form of smaller triangles on top of the average size triangles [see Fig. 1(b)]. An interesting domain boundary in the MoS₂ monolayer found by XTEM as a 10 nm overlap of the monolayers on each side as shown in the red inset of Fig. 1(b). Terraces of atomic planes and steps are found in the GaN lattice that are bridged by MoS₂ monolayers on top. EDX analysis done by *in-situ* XTEM reveals the presence of Mo or S line in the surface area where the top isolated plane is visible. The presence of Mo and S is not found in bulk GaN or on the surface of bare GaN, confirming that the isolated atomic plane in Fig. 1(b) is MoS₂.

XTEM images of monolayer MoS₂ (Samples A and B), bilayer MoS₂, and bare GaN are shown in Figure 2. For each XTEM image, corresponding intensity line profiles were taken in the direction perpendicular to the sample surface. Multiple intensity line profiles were taken in the area outlined by each yellow box, and the average intensity values were plotted in the graphs in Figure 2. Figures 2(a) and 2(b) show monolayer MoS₂/GaN heterojunctions, Fig. 2(c) shows a bilayer MoS₂/GaN heterojunction, and Fig. 2(d) shows a bare GaN surface. In every case, where MoS₂ is present, we always see two modified GaN layers of one GaN unit cell just below the MoS₂. The apparent modification of the top two GaN layers under MoS₂ could be attributed to partial oxidation¹⁷ during the MoS₂ growth process, or some form of surface reconstruction. A detailed elemental analysis of the material composition in the vdW interfacial layer requires techniques such as time-of-flight secondary ion mass spectrometry (TOF-SIMS),¹⁸ or electron energy loss spectroscopy (EELS),¹⁹ which is beyond the scope of this study. The intensity line profiles corresponding to each XTEM image in Fig. 2 clearly show the presence of the modified GaN termination layers even in Fig. 2(a), where the XTEM image is less conclusive to the eye. The MoS₂-GaN molecular layer spacing, $\Delta_{\text{M-G}}$, can be evaluated in the TEM images as the difference in the peaks 1 and 2 locations shown in the inset table in Figs. 2(a) and 2(b) [or peaks 2–3 in Fig. 2(c)] and consists of δ and half-layer thicknesses (θ_{MoS_2} , θ_{GaN}): $\Delta_{\text{M-G}} = \delta + \theta_{\text{MoS}_2}/2 + \theta_{\text{GaN}}/2$. δ is evaluated from the center-to-center for Ga and S atoms and θ_{GaN} is omitted in our case for Ga-terminated GaN. The MoS₂-GaN

spacing is measured with TEM in the range $\Delta_{M-G} = 3.8$ to 5.7 Å. The variation of Δ_{M-G} is possibly due to the bridging of the MoS₂ monolayer over the GaN terraces or different conditions of the GaN termination double-layer, which is more pronounced in Fig. 2(b) than in Fig. 2(a). That said, we note a $\Delta_{M-G} = 4.55$ Å peak-to-peak distance between the MoS₂ and the first GaN peak [peaks 2–3 in Fig. 2(c)]. This matches well to a value of 1.5 Å for the S-Mo bond distance ($\theta_{\text{MoS}_2}/2$) plus $\delta \sim 3.1$ Å, vdW gap between S and Ga at the interface, as predicted by our theoretical calculation [see Fig. 1(c)].

We use in-plane intensity line profiles (in the XTEM images not shown) to extract the in-plane lattice constants of MoS₂ and GaN. The in-plane line profiles are noisy, so we performed a fast Fourier transform (FFT) to accurately extract the amplitude versus inverse distance. From the FFT, we extract in-plane lattice constants of 3.19 ± 0.13 Å for MoS₂ and 3.15 ± 0.08 Å for GaN, i.e., with a lattice mismatch of 1.2%. The extracted lattice constants and mismatch align well with the published results on the lattice constant $a = 3.17$ Å of unstrained MoS₂ (Ref. 14) as well as our calculations.

To analyze the electrical properties of the 2D/3D heterojunction, the CAFM measurements are performed using the setup illustrated in Fig. 3(a). The current-voltage (*I-V*) characteristics measured by CAFM for MoS₂/*n*-GaN and MoS₂/*p*-GaN vertical heterojunctions as well as bare *n*-GaN and *p*-GaN are shown in Fig. 3(b). In these measurements, the CAFM tips are grounded and made of Pt-Ir, resulting in a Pt-Ir/MoS₂/GaN stack. The bias is applied to the substrate using a large top contact to GaN as justified previously.³ The CAFM electrical measurements on MoS₂ show clear rectifying behavior in *I-V*s for both *n*- and *p*-doped GaN substrates. The *I-V*s for MoS₂/*n*-GaN are nearly exponential with the current reduction at large biases due to the Ohmic voltage drop.³ The *I-V*s for MoS₂/*p*-GaN are non-exponential and show higher threshold voltages.

The analysis of the *I-V* data shown in Fig. 3(b) for MoS₂ on both *n*-GaN and *p*-GaN and comparison with the

measurements on bare GaN substrates provide a better understanding of the origin of the rectification behavior. There is a polarity change of the rectification when the substrate under MoS₂ changes from *n*-GaN to *p*-GaN. The rectification polarity for the MoS₂/*n*-GaN *I-V*s corresponds to either the tip/MoS₂ Schottky barrier, as argued in the earlier CAFM measurements on MoS₂,^{3,20} or tip/*n*-GaN Schottky barrier as supported in this study. On the other hand, the rectification polarity for the MoS₂/*p*-GaN *I-V*s coincides with the expected polarity in this *p-n* junction with MoS₂ being the *n*-type semiconductor. Similar *I-V*s and polarity were recently ascribed to the *p-n* junction behavior for *n*-MoS₂ on *p*-InGaIn.⁴ However, consideration of the *I-V* data for several tip-semiconductor cases in Fig. 3(b) indicates that the tip-GaN contact behavior governs the electrical transport rather than the MoS₂/GaN *p-n* junction. If the rectifying behavior for MoS₂/*n*-GaN is due to the tip-MoS₂ Schottky barrier, then this barrier should be present in the MoS₂/*p*-GaN *I-V* curves which would zero the *I-V* at positive bias, which is not observed in Fig. 3(b). In addition, the *I-V*s for bare GaN resemble the *I-V*s for the MoS₂/GaN heterojunction in polarity and shape. These data can be reconciled if we assume that the *I-V*s are governed by the tip-GaN junction which is modified by the presence of an MoS₂ monolayer. These results are important to consider when building vertical *p-n* junction heterostructures involving 2D crystals as illustrated with the variation of *I-V* interpretations mentioned above. The 2D semiconductor components below a certain thickness in vertical bipolar heterojunctions might be electronically transparent and introduce only superficial changes to the electron transport instead of acting as independent semiconductor components.

For both types of GaN layers, the insertion of the MoS₂ layer reduces the magnitude of the turn-on voltage, which is especially pronounced for the MoS₂/*n*-GaN case. In order to understand how the 1L-MoS₂ layer modifies the electrical properties of the Pt-Ir/*n*-GaN junction, we performed a DFT calculation of the work function and conduction and valence band offsets of the 1L-MoS₂/*n*-GaN interfacial layer (MSGN) as well as bulk Pt and *n*-GaN, using the methods and parameters described earlier in this paper. The bulk Pt layer model was created by following the recipe of the bulk GaN model described above. The MSGN layer is of approximately 2.2 nm thickness and includes 0.4 nm of MoS₂ monolayer, 0.3 nm of vdW gap, and 1.5 nm of bulk-like GaN slab. The band alignments of the MSGN interfacial layer versus Pt and bulk GaN are displayed in Fig. 3(c). The bandgap 1.86 eV and electron affinity 4.3 eV of the MoS₂/GaN interface are found to be close to the DFT-calculated values for the 1L-MoS₂. In order to compare the Schottky barrier heights (SBHs) of the Pt/*n*-GaN junction and the double junction of Pt/MSGN and MSGN/*n*-GaN, the SBHs are estimated using the Schottky-Mott approximation as the difference between the metal work function and the semiconductor electron affinity. The insertion of the 1L-MoS₂ causes the reduction of the SBH from 1.4 eV for Pt/GaN to 1.2 eV for Pt/MSGN. Moreover, because of the ultrathin dimension of the MSGN layer, it will be susceptible to increased electron tunneling and larger currents. The difference in the electron affinity of 0.2 eV between the MGSN and bulk-GaN contributes to the

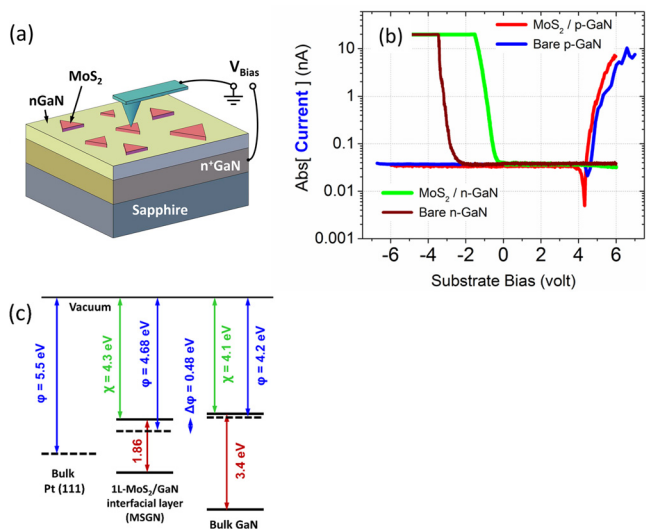


FIG. 3. (a) Illustration of heterojunction sample and CAFM measurement. (b) Current-voltage characteristics measured with CAFM for MoS₂/*n*-GaN and MoS₂/*p*-GaN heterojunctions and bare *n*-GaN and *p*-GaN surfaces. (c) DFT-calculated band alignment of Pt (111) surface, bulk *n*-GaN, and 1L-MoS₂/GaN interfacial layer (MSGN).

formation of a secondary barrier, where MSGN forms a graded junction. Hence, the reduction of the SBH and the formation of a secondary potential barrier due to the introduction of 1L-MoS₂ collectively contribute to the overall increase in the current and reduce the turn-on voltages as observed in Fig. 3(b). Small thickness of the interfacial MSGN layer must be the reason of the similarity of the *I-V* curves with and without 1L-MoS₂ especially for the case of *p*-GaN, where the electrical data indicate no apparent *p-n* junction. Future DFT calculations of the Fermi level position for the full metal/1L-MoS₂/GaN stack aim to provide further insight.

In conclusion, we performed XTEM of monolayer MoS₂ on GaN vertical heterojunctions that were grown by the powder vaporization technique. The extracted in-plane lattice constants of GaN and MoS₂ were similar to those of bulk unstrained values, indicating an epitaxial, nearly lattice-matched growth of MoS₂ on GaN. The interlayer vdW gap of ~ 3.1 Å between GaN and monolayer MoS₂ that we extracted from XTEM images is consistent with the theoretically predicted vdW gap. We used CAFM to measure vertical current across the MoS₂/*n*-GaN and MoS₂/*p*-GaN heterojunctions and observed rectification of the current in both cases as well as a switch of the polarity of the rectification for *n*- and *p*-doped GaN. There is a larger turn-on voltage shift due to the insertion of MoS₂ for the *n*-GaN case that may be explained by Schottky barrier lowering and the formation of a graded junction. Despite the fact that an unperturbed single layer MoS₂ is distinctly observed on the GaN surface by XTEM, our electrical measurements and theoretical analysis indicate that the monolayer does not demonstrate bulk semiconductor properties and can be viewed as a modified nanoscale interface in the vertical metal/GaN junction. This may open up possibilities for the engineering 2D/3D heterojunction for the future technologies. For the purpose of building vertical bipolar devices with independent MoS₂ components, stacks of multiple 2D layers would be needed.

This work was supported by the U.S. Army Research Laboratory (ARL) Director's Strategic Initiative (DSI) program on understanding and exploiting the electronic interface in stacked 2D atomic layered materials. This work is supported by grants of computer time from DOD High

Performance Computer Modernization Program at the U.S. Air Force Research Laboratory and U.S. Army Engineer Research and Development Center DoD Supercomputing Resource Centers. D.R. and A.V.D. acknowledge the support of Material Genome Initiative funding allocated to NIST. K.Z. and J.A.R. acknowledge the Center for Atomically Thin Multifunctional Coatings (ATOMIC), sponsored by the National Science Foundation (NSF) division of Industrial, Innovation and Partnership (IIP) under Award No. #1540018.

- ¹B. Dubertret, T. Heine, and M. Terrones, *Acc. Chem. Res.* **48**(1), 1 (2015).
- ²Y.-H. Lee, L. Yu, H. Wang, W. Fang, X. Ling, Y. Shi, C.-T. Lin, J.-K. Huang, M.-T. Chang, C.-S. Chang, M. Dresselhaus, T. Palacios, L.-J. Li, and J. Kong, *Nano Lett.* **13**, 1852 (2013).
- ³D. Ruzmetov, K. Zhang, G. Stan, B. Kalanyan, G. R. Bhimanapati, S. M. Eichfeld, R. A. Burke, P. B. Shah, T. P. O'Regan, F. J. Crowne, A. G. Birdwell, J. A. Robinson, A. V. Davydov, and T. G. Ivanov, *ACS Nano* **10**, 3580 (2016).
- ⁴K. Jung, C. Y. Liu, J. D. Kim, W. Choi, W. Zhou, H. C. Kuo, and X. Li, in *2016 IEEE Photonics Conference IPC* (2016), pp. 657–658.
- ⁵Z. Chen, H. Liu, X. Chen, G. Chu, S. Chu, and H. Zhang, *ACS Appl. Mater. Interfaces* **8**, 20267 (2016).
- ⁶B. Kiraly, R. M. Jacobberger, A. J. Mannix, G. P. Campbell, M. J. Bedzyk, M. S. Arnold, M. C. Hersam, and N. P. Guisinger, *Nano Lett.* **15**, 7414 (2015).
- ⁷S. Krishnamoorthy, E. W. L. Li, C. H. Lee, Y. Zhang, W. D. McCulloch, J. M. Johnson, J. Hwang, Y. Wu, and S. Rajan, *Appl. Phys. Lett.* **109**, 183505 (2016).
- ⁸J. C. Bravman and R. Sinclair, *J. Electron Microsc. Tech.* **1**, 53 (1984).
- ⁹P. E. Blöchl, *Phys. Rev. B* **50**, 17953 (1994).
- ¹⁰G. Kresse and J. Furthmüller, *Phys. Rev. B* **54**, 11169 (1996).
- ¹¹J. P. Perdew, K. Burke, and M. Ernzerhof, *Phys. Rev. Lett.* **77**, 3865 (1996).
- ¹²H. J. Monkhorst and J. D. Pack, *Phys. Rev. B* **13**, 5188 (1976).
- ¹³S. Grimme, *J. Comput. Chem.* **27**, 1787 (2006).
- ¹⁴V. Petkov, S. J. L. Billinge, P. Larson, S. D. Mahanti, T. Vogt, K. K. Rangan, and M. G. Kanatzidis, *Phys. Rev. B* **65**, 092105 (2002).
- ¹⁵V. Darakchieva, B. Monemar, and A. Usui, *Appl. Phys. Lett.* **91**, 031911 (2007).
- ¹⁶K. Kang, S. Xie, L. Huang, Y. Han, P. Y. Huang, K. F. Mak, C.-J. Kim, D. Muller, and J. Park, *Nature* **520**, 656 (2015).
- ¹⁷N. J. Watkins, G. W. Wicks, and Y. Gao, *Appl. Phys. Lett.* **75**, 2602 (1999).
- ¹⁸H. Chou, A. Ismach, R. Ghosh, R. S. Ruoff, and A. Dolocan, *Nat. Commun.* **6**, 7482 (2015).
- ¹⁹J. A. Taillon, J. H. Yang, C. A. Ahyi, J. Rozen, J. R. Williams, L. C. Feldman, T. S. Zheleva, A. J. Lelis, and L. G. Salamanca-Riba, *J. Appl. Phys.* **113**, 044517 (2013).
- ²⁰F. Giannazzo, G. Fisichella, A. Piazza, S. Agnello, and F. Roccaforte, *Phys. Rev. B* **92**, 081307 (2015).